

# **Final Report for MEng Individual Project**

---

## **Deep learning $T_2$ mapping in MRI using phase-cycled bSSFP signals**

---

**Author Name:** Yi Teng Voon

**CID:** 01411911

**Supervisor:** Dr Neal Bangerter

**Submitted in partial fulfilment of the requirements for the award of MEng in Biomedical Engineering from Imperial College London**

**June 2021**

**Word Count: 4651**

## Abstract

Quantitative MR imaging such as  $T_2$  mapping plays an important role as a non-invasive biomarker for clinical and research purposes. Constructing  $T_2$  maps from magnitude images obtained using traditional spin-echo method is difficult in low SNR environments and time-prohibitive. Parametric approaches like PLANET have been developed for rapid  $T_2$  mapping from phase-cycled images acquired using fast scanning techniques such as bSSFP. However, the accuracy of PLANET suffers when short phase-cycled, highly noise-corrupted bSSFP signals are used. In this work, deep learning methods for  $T_2$  estimation from simulated phase-cycled bSSFP signals in brain tissues are proposed as faster and better alternatives to PLANET. Extensive datasets derived from existing bSSFP simulations are modified to train a voxel-based and an image-based supervised regression neural network. The performance of two regression networks and PLANET are compared over a broad range of SNR. For simulated data, the trained regression networks are demonstrated to have  $T_2$  predictions that are closer to the true  $T_2$  than PLANET. Voxel-based regression network is found to have a relatively higher accuracy and precision of  $T_2$  predictions than image-based regression network. Despite a lower prediction precision, image-based regression network shows great potential for  $T_2$  mapping with its capability to process spatial information from phase-cycled bSSFP images. The limitations of both regression networks and future improvements to address them are also discussed.

## Acknowledgement

I would like to express my heartfelt gratitude to my project supervisor Dr Neal Bangerter for his exceptional support and valuable guidance throughout the project. I am also thankful to Michael and Jiaxin for providing much needed materials for this project. Lastly, I am grateful to my friends and family for everything they have done to help me through my undergraduate degree.

# Contents

|                 |  |           |
|-----------------|--|-----------|
| <b>1</b>        | <b>Introduction</b>  | <b>4</b>  |
| 1.1             | Background . . . . .   | 4         |
| 1.2             | Motivation . . . . .   | 6         |
| 1.3             | Aim and Objectives . . . . .   | 6         |
| <b>2</b>        | <b>Methods</b>   | <b>7</b>  |
| 2.1             | Data Preparation . . . . .   | 7         |
| 2.2             | Voxelwise Regression . . . . .                                       | 8         |
| 2.2.1           | Architecture . . . . .   | 8         |
| 2.2.2           | Training Parameters . . . . .  | 9         |
| 2.3             | Image-to-image Regression . . . . .                                  | 9         |
| 2.3.1           | Architecture . . . . .   | 9         |
| 2.3.2           | Training Parameters . . . . .  | 10        |
| 2.4             | Evaluation Methods . . . . .   | 10        |
| <b>3</b>        | <b>Results</b>   | <b>11</b> |
| 3.1             | Voxelwise Regression . . . . .                                       | 11        |
| 3.2             | Image-to-image Regression . . . . .                                  | 13        |
| <b>4</b>        | <b>Discussion</b>  | <b>15</b> |
| <b>5</b>        | <b>Conclusion</b>  | <b>16</b> |
| <b>6</b>        | <b>References</b>  | <b>17</b> |
| <b>Appendix</b> |  | <b>19</b> |
| A               | Functions of the layers used for image-to-image regression . . . . . | 19        |
| B               | PDFs for 6 phase cycles . . . . .                                    | 20        |

# 1 Introduction

## 1.1 Background

In magnetic resonance (MR) imaging, scan images are acquired by taking the magnitude of the complex-valued radio frequency (RF) signals received from a region of interest in a subject after the subject is excited by RF pulses. The signal magnitude decays exponentially with a tissue-dependent time constant  $T_2$  and it is read at different times after excitations called echo time (TE). A useful quantitative imaging technique known as  $T_2$  mapping is often used to characterize tissue types by constructing a parametric map with a single  $T_2$  value per pixel. A deviation from a normal  $T_2$  value in tissues is an effective biomarker of pathologies in diseases like osteoarthritis (OA), in which the lengthening of  $T_2$  values indicates cartilage degeneration [1] (Figure 1).

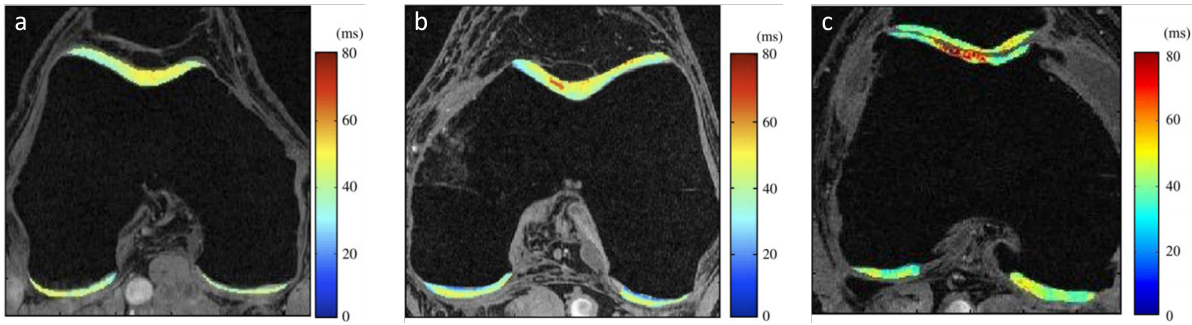


Figure 1: Axial knee scans of patients with (a) Healthy cartilage, (b) Mild OA and (c) Severe OA in the femoral-tibial and femoral-patellar joints. Lengthening  $T_2$  is shown in the colour changes from green to red [2]

The ability to detect  $T_2$  anomalies makes  $T_2$  mapping a particularly important visualization tool for clinical diagnosis. Conventionally, gold standard  $T_2$  mapping is achieved from 5 to 6 magnitude images acquired using a scanning technique known as Multi-Echo Spin Echo (ME-SE). Unfortunately, scans based on ME-SE require a long acquisition time to generate sufficient images for accurate  $T_2$  mapping, which makes the traditional technique time-costly to perform at high-resolution imaging. Therefore, the utility of  $T_2$  mapping is often limited to 2D multi-slice acquisitions with a limited number of slices. Recovering  $T_2$  distributions from low signal-to-noise ratio (SNR) multi-echo measurements is also challenging because noise bias can significantly alter  $T_2$  values (Figure 2).

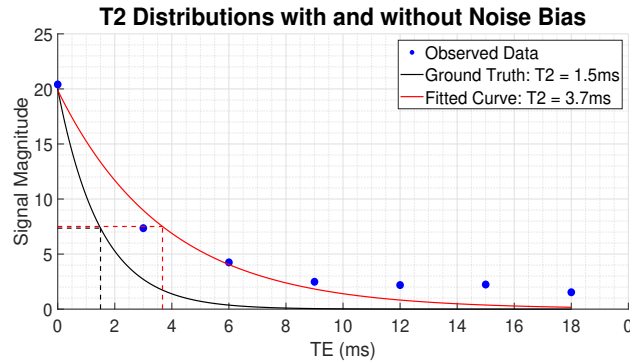


Figure 2:  $T_2$  distributions with (red) and without noise bias (black)

With recent advances in MRI systems, another scanning technique known as balanced steady-state free precession (bSSFP), is now widely used for rapid imaging due to its relatively fast scan time. However, bSSFP is very susceptible to noise corruption which can reduce SNR of the signals substantially. Another limitation of bSSFP signals is that they are highly sensitive to off-resonance frequencies arising from magnetic field inhomogeneity, which can cause patterned signal voids known as banding artifacts to appear on bSSFP images [3]. Through a process called phase cycling, in which the phase of the excitation pulse is incremented, multiple bSSFP images can be generated and then combined to suppress banding artifacts. In an attempt to completely remove banding artifacts, Xiang and Hoff (2014) introduced an elliptical model that fits a set of phase-cycled bSSFP signals in the complex plane, which ultimately allows reconstruction of banding free bSSFP images [4] (Figure 3).

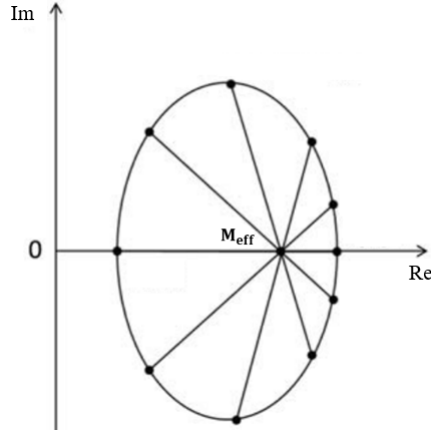


Figure 3: *Elliptical signal model by Xiang and Hoff. The dots on the ellipse represent the phase-cycled bSSFP signals and the amount of the dots represents the number of phase cycles. The model allows computation of an elliptical cross point that represents the effective signal magnitude,  $M_{\text{eff}}$ , which can be expressed as a weighted sum of two pairs of magnitude images and be used to reconstruct bSSFP images without banding artifacts [4]*

A parametric approach to approximate an analytical solution for  $T_2$  named PLANET was proposed by Shcherbakova et al. (2017). PLANET performs linear least squares fitting to a set of phase-cycled bSSFP signals modelled by Xiang and Hoff's elliptical distribution [5]. Mathematically, PLANET fits the following polynomial function to phase-cycled bSSFP signals where  $x$  and  $y$  are the real and imaginary components of the signals respectively:

$$F(C, x) = C_1x^2 + C_2xy + C_3y^2 + C_4x + C_5y + C_6 = 0 \quad (1)$$

Shcherbakova's team showed promising results on  $T_2$  mapping from 10 phase-cycled bSSFP signals. However, PLANET computes  $T_2$  values that are far from the nominal  $T_2$  values when noise is large. While the number of unknowns in Equation 1 implies that the input for PLANET could theoretically be reduced to 6 phase-cycled bSSFP signals, the scan time required to produce 6 inputs remains a limitation even with bSSFP. Another drawback of PLANET is that a new solution is needed for each new set of phase-cycled bSSFP signals, which significantly increases the computational time for a large set of data.

## 1.2 Motivation

In recent years, researchers see successful implementations of deep learning methods for fast  $T_2$  mapping. One such example is the rapid  $T_2$  map construction from undersampled  $T_2$ -weighted brain images using a neural network developed by Meng et al. (2020) trained with a large amount of images [6]. A previous Imperial College London student has developed a bSSFP simulation which allows generation of phase-cycled bSSFP signals at a large scale, with emulation of noise corruption and banding effects [7]. Through his simulation, phase-cycled bSSFP signals can be presented in the form of arrays or images, which can be used to train a corresponding type of supervised regression neural network to predict  $T_2$  values:

- (i) **Voxelwise regression**, a non-linear neural network trained with arrays of phase-cycled bSSFP signals to estimate a single  $T_2$  value
- (ii) **Image-to-image regression**, a convolutional neural network (CNN) trained with series of phase-cycled bSSFP images to predict a complete  $T_2$  map

There are two major advantages of employing neural networks over PLANET for  $T_2$  mapping using phase-cycled bSSFP signals. First,  $T_2$  estimation for a huge set of signals is faster with trained neural networks than PLANET. Second, the input required for neural networks can potentially be further decreased by reducing the degree of freedom using low-rank approximation methods such as principal component analysis (PCA) [8], and thus shortening image acquisition time.

## 1.3 Aim and Objectives

The aim of this project is to implement deep learning methods to achieve faster and more robust  $T_2$  mapping using phase-cycled bSSFP signals. In order to achieve the aim, the objectives of this project include (i) designing voxelwise and image-to-image regression neural networks based on array and image representations of phase-cycled bSSFP input respectively, (ii) training the neural networks with different numbers of phase cycles, SNR ranges and degrees of banding artifacts, (iii) comparing  $T_2$  output computed by the neural networks and PLANET in terms of probability density functions (PDF), and (iv) evaluating the neural networks for  $T_2$  mapping from bSSFP signals with different phase cycles and SNR levels.

## 2 Methods

### 2.1 Data Preparation

A human brain phantom developed by BrainWeb is used for phase-cycled bSSFP signals simulation [9]. The original phantom is of image size  $128 \times 128$  pixels where each pixel contains a number from 1 to 11 corresponding to 11 classes of tissue found in the brain. Two tissue types are selected for the purpose of the project: gray matter (GM) and white matter (WM). GM is composed of neurons and WM includes long nerve axons and their protective layers of fat. In practice, the measured  $T_2$  values of GM and WM are dependent on intrinsic factors like the age [10], location of the tissue in the brain [11], and extrinsic factors such as the main magnetic field strength  $B_0$ , the type of scanning technique used and the SNR of the received RF signals. Using a 3T MRI scanner, GM is reported to have  $T_2$  ranging from  $80ms$  to  $130ms$  while WM has a  $T_2$  range of  $70 - 90ms$  [12][13]. For this project, nominal  $T_2$  of  $100ms$  and  $80ms$  are set as the ground truths  $T_2$  for GM and WM respectively. Based on the nominal  $T_2$ , a ground truth  $T_2$  map is generated. To reduce training time, the ground truth  $T_2$  map is resized to  $40 \times 28$  pixels, with the field-of-view (FOV) focusing on the lateral ventricles of the brain (Figure 4).

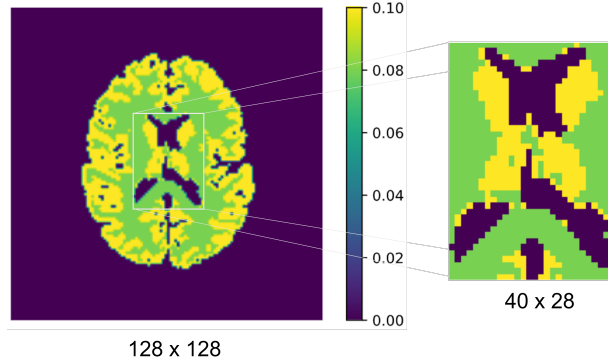


Figure 4: *Ground truth  $T_2$  map ( $128 \times 128$  pixels) and its cropped version ( $40 \times 28$  pixels), yellow region represents GM and green region represents WM*

For the bSSFP simulation, fixed MR parameters such as  $B_0$ , relaxation time TR and flip angle  $\alpha$  are set as 3T,  $1ms$  and  $30^\circ$  respectively. The independent variables for the simulations are the number of phase cycles, off-resonance frequency, and standard deviation of Gaussian noise. 8 and 6 phase cycles are trained and tested with both voxelwise and image-to-image regression. Off-resonance frequency is sampled from a uniform distribution of floating points between 0 and  $300Hz$  to emulate banding artifacts of varying frequencies. Banding artifacts are also irregularly rotated and deformed. To generate bSSFP signals with different SNR ranges, the standard deviation of Gaussian noise is varied between 0.001 and 0.02. Unlike the Gaussian noise associated with the RF signals received from the tissues, the noise in the background of the image where signals are absent follows a Rayleigh distribution instead, which is a skewed version of the Gaussian model [14]. The SNR is calculated by dividing the mean signal magnitude from tissues of interest over Rayleigh-corrected standard deviation of background noise:

$$SNR = \frac{SM_{mean}}{\sigma_{rayleigh}} \quad (2)$$

GM has a SNR range of 6 - 150 and WM has a SNR range of 6 - 160 when the standard deviation of Gaussian noise is in the range of 0.001 - 0.02.

Simulated bSSFP images for 8 phase cycles are concatenated columnwise and the final form of the input used for image-to-image regression is a  $40 \times 224$  pixels image (Figure 5).

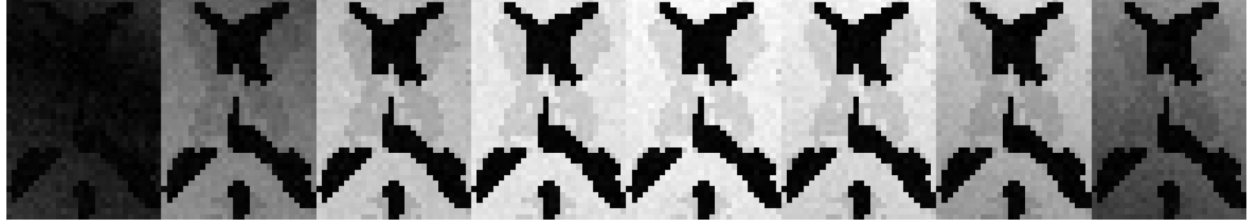


Figure 5: *Concatenated 8 phase-cycled bSSFP images*

The images are represented by the magnitudes of complex-valued signals. For a particular point in a set of 8 phased-cycled bSSFP images, the signals can be arranged in an 8-element array in which each element is a complex number:

$$\begin{bmatrix} x_1 + iy_1 & x_2 + iy_2 & x_3 + iy_3 & x_4 + iy_4 & x_5 + iy_5 & x_6 + iy_6 & x_7 + iy_7 & x_8 + iy_8 \end{bmatrix}$$

The input for voxelwise regression is the expanded version of such array with the real and imaginary parts split into 16 elements:

$$\begin{bmatrix} x_1 & y_1 & x_2 & y_2 & \dots & x_7 & y_7 & x_8 & y_8 \end{bmatrix}$$

The preparation for 6 phase-cycled input follows the same approach.

## 2.2 Voxelwise Regression

A multilayer perceptron (MLP) is used to predict  $T_2$  from arrays of phase-cycled bSSFP signals, in which the weighted sum of the input is mapped to the output by fully-connected hidden layers with activation functions.

### 2.2.1 Architecture

To select the structure of the network, different networks with varying number of hidden layers (4-6) and number of neurons per layer (64, 128, 256) are tested. 6 hidden layers and 256 neurons are selected as this configuration had the lowest validation loss at the end of training. As a whole, the network is composed of an input layer with 16 units, 6 hidden layers of 256 neurons each and a single output unit. All the hidden layers use a leaky rectified linear function (Leaky ReLu) as the activation function, except for the final hidden layer which uses a linear activation function to allow the output to be computed as a continuous number instead of a discrete class. This architecture is for 8 phase cycles, but adjustments are made to fit 6 phase-cycled bSSFP signals.

### 2.2.2 Training Parameters

100,000 arrays of phased-cycled bSSFP signals are simulated for the network, 80% of which is for training, 10% is reserved as validation set and the remaining 10% is used as the testing set for evaluation. The signal array input is normalized before being passed into the network. The mean squared error (MSE) between the prediction  $\hat{T}_2$  and the target  $T_2$  is chosen as the loss function, as described in Equation 2 where N is the total number of arrays for training with each array indexed by i:

$$Loss = \frac{1}{N} \sum_{i=1}^N (\hat{T}_2 - T_2)^2 \quad (3)$$

Adam optimizer with a learning rate of 1E-03 and a batch size of 10 are used. The network is trained for 10 epochs and takes approximately 1 minute to complete, showing the feasibility for model retraining and fine-tuning given a large database of signals. The network is built and trained in TensorFlow 2.0 on Python 3.6 environment with an Intel i5-8250U CPU.

## 2.3 Image-to-image Regression

The end-to-end image approach predicts a complete  $T_2$  map from phase-cycled bSSFP images based on U-Net, a type of CNN which takes images as input, captures the local and global information of the images through a series of operations, and produces an output connecting all the extracted features.

### 2.3.1 Architecture

The U-Net architecture for image-to-image regression using 8 phase-cycled bSSFP images comprises two main paths (Figure 6).

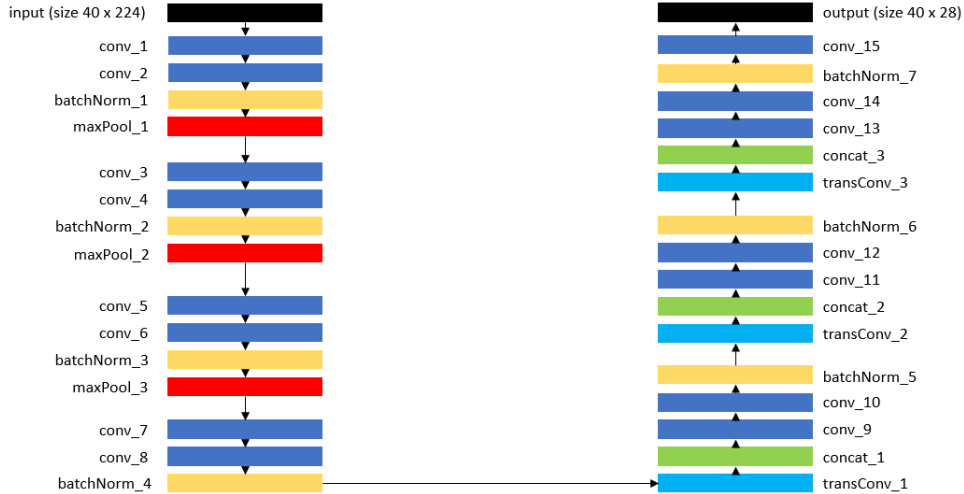


Figure 6: *U-Net architecture for image-to-image regression using 8 phase-cycled bSSFP images*

The first path is the downsampling or encoding path, which is used to extract features from the image. The encoder is usually made up of stacks of convolutional, batch normalisation and max pooling layers. In this case, the initial part of the downsampling path consists of 3 stacks of the layer combination: 2 consecutive convolutional layers, 1 batch normalisation and 1 max pooling layer. The last layer that is connected to the second path is slightly different, having only 2 successive convolutional layers and 1 batch normalisation layer.

The second path is the upsampling or decoding path, which is used to enable precise reconstruction based on extracted features using transposed convolutions. The decoder consists of 3 stacks of such layer combination: 1 transposed convolutional layer, 1 concatenating layer, 2 successive convolutional layers and 1 batch normalisation layer. They connect to the final layer, which is a single convolutional layer that resize the output to the size of the ground truth  $T_2$  map.

The two paths link together, forming a CNN for phase-cycled bSSFP images with a total of 15 convolutional layers, 7 batch normalisation, 3 max pooling, 3 transposed convolution and 3 concatenating layers. The functions of each layer used are given in Appendix A. The U-Net architecture for 8 phase cycles is demonstrated. There are slight adjustments on the architecture to fit 6 phase-cycled bSSFP images.

### 2.3.2 Training Parameters

Similar to voxelwise regression, the loss function is the MSE. The Adam optimizer with a learning rate of 1E-03 and a batch size of 10 is used. Due to the limitation of the hardware, only 1000 sets of phase-cycled images are used for input, 80% for training, 10% for validation and 10% for testing. Training runs for 30 epochs, which takes about 3 minutes.

## 2.4 Evaluation Methods

The voxelwise and image-to-image regression networks are trained and tested at three different levels of SNR range: Low ( $< 20$ ), Medium ( $20 - 100$ ) and High ( $> 100$ ). The test MSE of voxelwise and image-to-image regression is used to measure the accuracy. Furthermore, Monte Carlo simulation is performed on the predicted  $T_2$  from the testing set for the regression networks to obtain PDFs for GM and WM. The same testing sets are also used to generate PDFs for PLANET. Means and standard deviations of predicted  $T_2$  are obtained from the PDFs. The differences between the nominal and mean predicted  $T_2$  are used to compare the prediction accuracy, whereas the standard deviations are used to compare the precision of the two regression networks and PLANET in different SNR levels

To address the issue of PLANET predicting  $T_2$  that are far off the nominal  $T_2$  in the presence of large noise, an acceptable  $T_2$  range of  $70 - 120ms$  is set for both GM and WM.  $T_2$  values predicted by PLANET that are out of this range are rejected, which ensures that the mean and standard deviation of  $T_2$  values predicted using PLANET is comparable to those of the neural networks. PLANET rejection rate is calculated by dividing the amount of samples fall between  $70 - 120ms$  over the total number of samples for GM and WM respectively. For image-to-image regression, the ground truth  $T_2$  map and mean predicted  $T_2$  maps of the test set in various SNR ranges are shown for comparison between 8 and 6 phase-cycles.

### 3 Results

The Python code for the bSSFP data preparation and implementation of voxelwise regression and image-to-image regression can be found on this Github link (<https://github.com/yv17/FYP-Python>).

#### 3.1 Voxelwise Regression

The testing set of voxelwise regression contains a total of 10,000 arrays of 8 phase-cycled bSSFP signals. Test MSEs of 5.00E-05, 5.02E-06 and 5.22E-07 are yielded for low, medium and high SNR level respectively, showing a ten-fold increase in accuracy of the network as SNR level increases. The PDFs of the predicted  $T_2$  from the voxelwise regression and PLANET for GM and WM in different SNR levels are plotted (Figure 8).

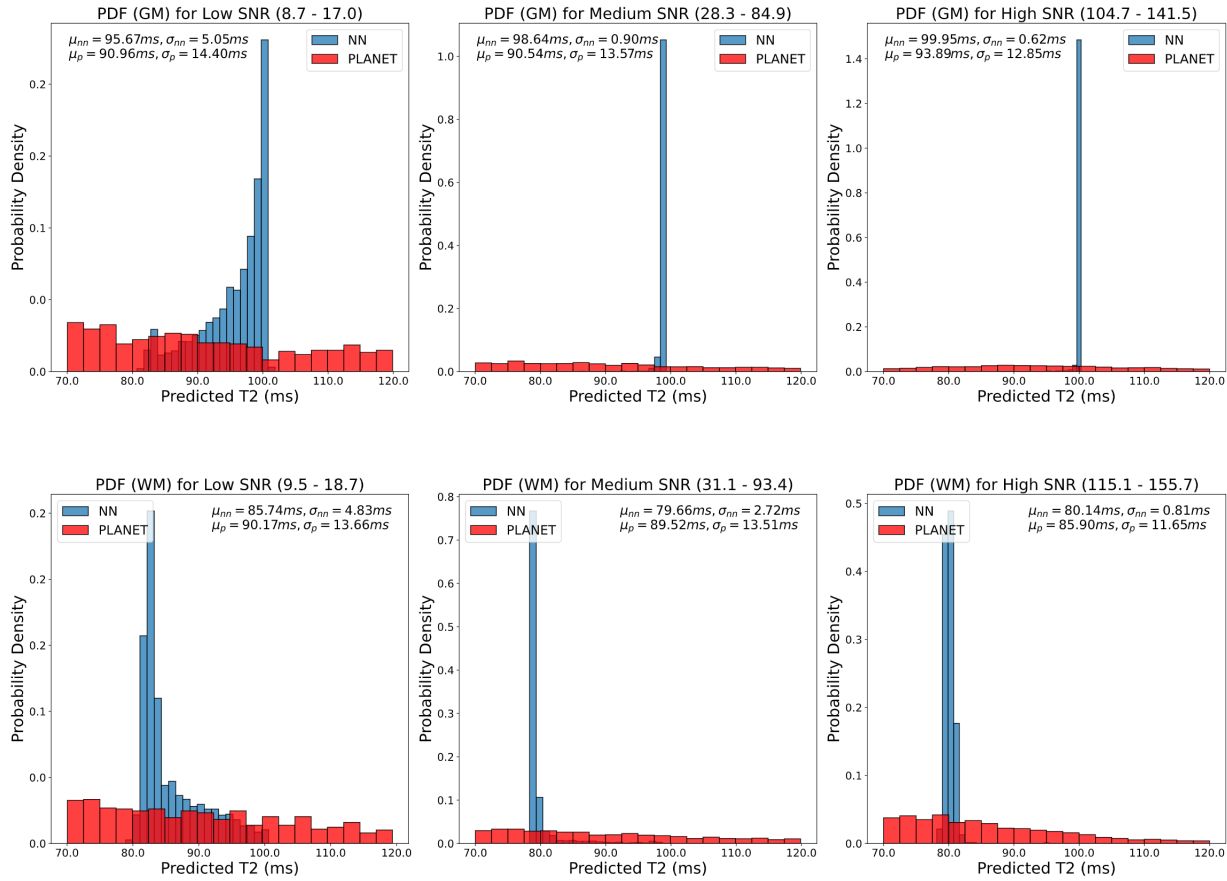


Figure 8: *GM and WM PDFs of predicted  $T_2$  from PLANET (red) and voxelwise regression (blue) for 8 phase-cycled bSSFP signals in different SNR levels. In medium and high SNR level, it is difficult to discern the PDFs of PLANET from the PDFs of voxelwise regression since the peaks of neural networks PDFs rise sharply at the nominal  $T_2$  as the standard deviations become very small*

For low SNR, the mean predicted  $T_2$  value is about 5ms off the nominal  $T_2$  for both GM and WM (100ms and 80ms), while for medium and high SNR levels, the mean predicted  $T_2$  values are within  $\pm 2\text{ms}$ . Across all levels of SNR, PLANET predicts  $T_2$  values that are at least more than 5ms away from the nominal  $T_2$ . PLANET has standard deviations that are at least 2 times larger than those of voxelwise regression in low

and medium SNR levels. In high SNR level, the standard deviation of PLANET is about 18 times larger than that of voxelwise regression as the standard deviation of voxelwise regression decreases significantly. The large differences in standard deviations show that  $T_2$  predictions of voxelwise regression are much more precise than those of PLANET in all SNR levels.

The PLANET PDFs do not have an expected bell curve centered about the nominal  $T_2$  of GM and WM in low and medium SNR levels because a large proportion ( $> 35\%$ ) of PLANET results are rejected when  $\text{SNR} < 100$  (Figure 9).

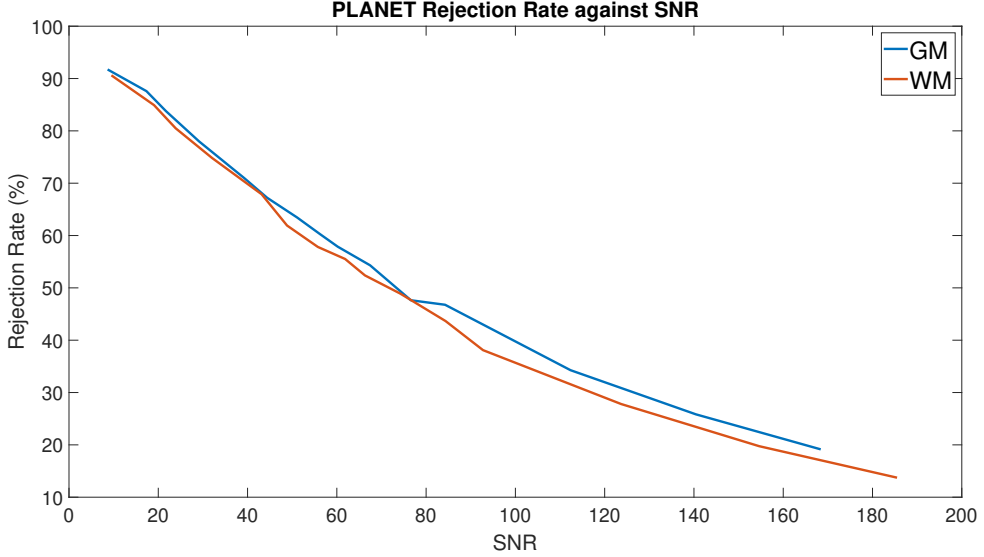


Figure 9: *PLANET* rejection rate for GM (blue) and WM (orange) from low to high SNR

Upon closer inspection, the PDFs for GM and WM start to resemble a normal distribution about their nominal  $T_2$  as the SNR rises above 100 and the rejection rate of computed  $T_2$  using PLANET falls below 35%.

The voxelwise regression network is also trained and tested with 6 phase-cycled bSSFP signals. Test MSEs of 6.53E-05, 6.83E-06 and 3.38E-07 are obtained for low, medium and high SNR levels respectively. The PDFs of voxelwise regression and PLANET for 6 phase-cycled bSSFP signals at different SNR levels are included in Appendix B. The mean predicted  $T_2$  of voxelwise regression are within  $\pm 5ms$  for low SNR level and  $\pm 3ms$  for medium and high SNR levels, which are nearly the same as the results for 8 phase cycles. The standard deviations of voxelwise regression are still at least 2 times smaller than those of PLANET, which shows that voxelwise regression works well even with 6 phase-cycled bSSFP signals, proving the feasibility of the neural network when used with the minimum number of inputs for PLANET. PLANET predictions are slightly worse in 6 phase cycles compared with 8 phase cycles, which is anticipated since fewer phase cycles will lead to higher failure rates of fitting phase-cycled bSSFP signals to the elliptical distribution in the presence of noise.

### 3.2 Image-to-image Regression

100 sets of 8 phase-cycled bSSFP images are used in the testing set for image-to-image regression. The test MSEs are 7.44E-05, 7.20E-05 and 9.17E-05 for low, medium and high SNR levels respectively. It is surprising that the test MSEs in low and medium SNR levels are of the same order as in high SNR, however it is noted that the MSEs can vary drastically in different repetitions of training. The PDFs of predicted  $T_2$  from image-to-image regression are compared to those from PLANET (Figure 11).

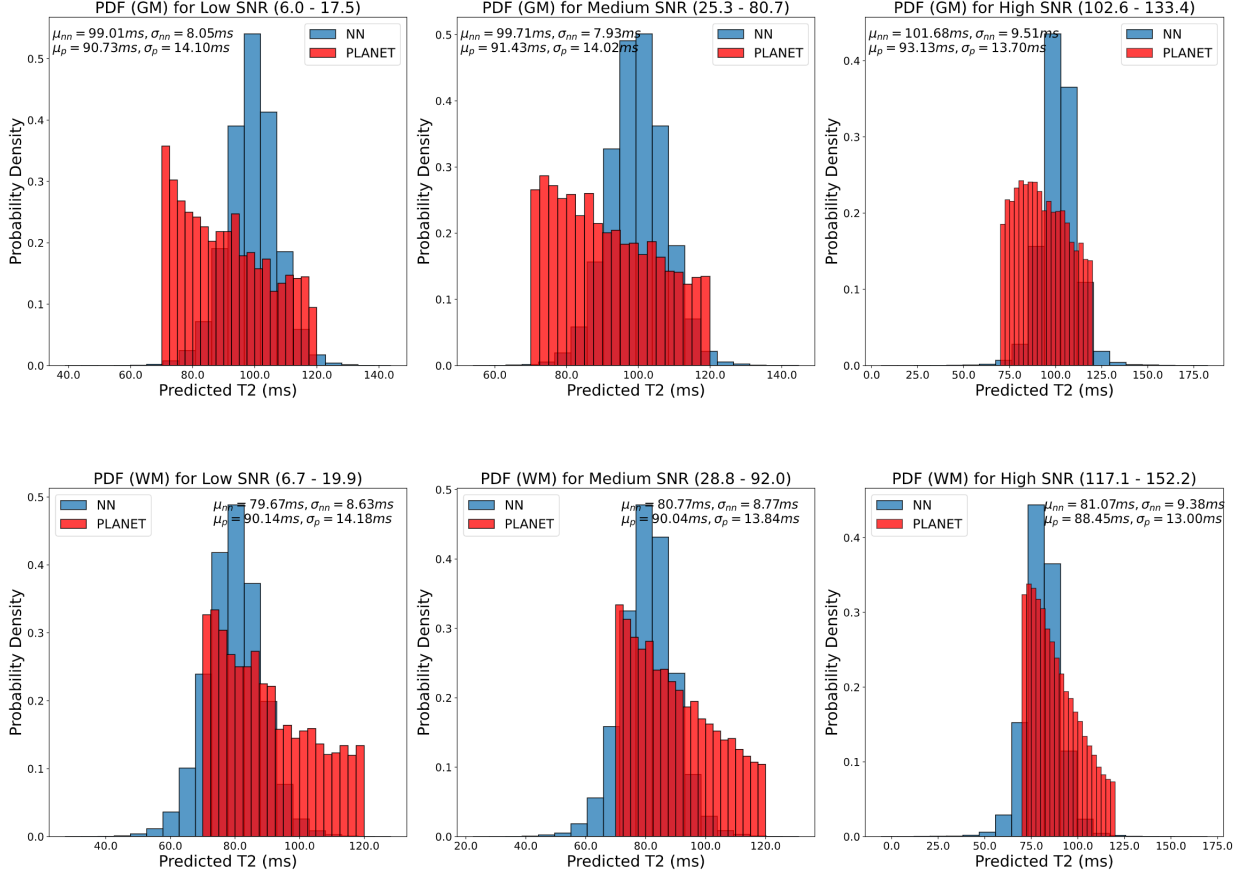


Figure 11: GM and WM PDFs of predicted  $T_2$  from PLANET (red) and image-to-image regression (blue) for 8 phase-cycled bSSFP images in different SNR levels

Across all SNR levels, the mean predicted  $T_2$  values of image-to-image regression are within  $\pm 2$ ms from the nominal  $T_2$ , as opposed to PLANET which are at least more than 6ms away. Image-to-image regression has standard deviations that are approximately half of the standard deviations of PLANET, which indicates that image-to-image regression has a higher prediction accuracy and precision than PLANET over a wide range of SNR.

In comparison with voxelwise regression, image-to-image regression obtains mean predicted  $T_2$  values that are marginally closer to the nominal  $T_2$  in low and medium SNR levels. However, the standard deviations of image-to-image regression are much higher than those of voxelwise regression in all SNR levels, indicating that image-to-image regression has a significantly lower precision than voxelwise regression.

The differences between the ground truth and the mean predicted  $T_2$  maps from 8 phase-cycled bSSFP images in low, medium and high SNR levels can be observed below (Figure 12).

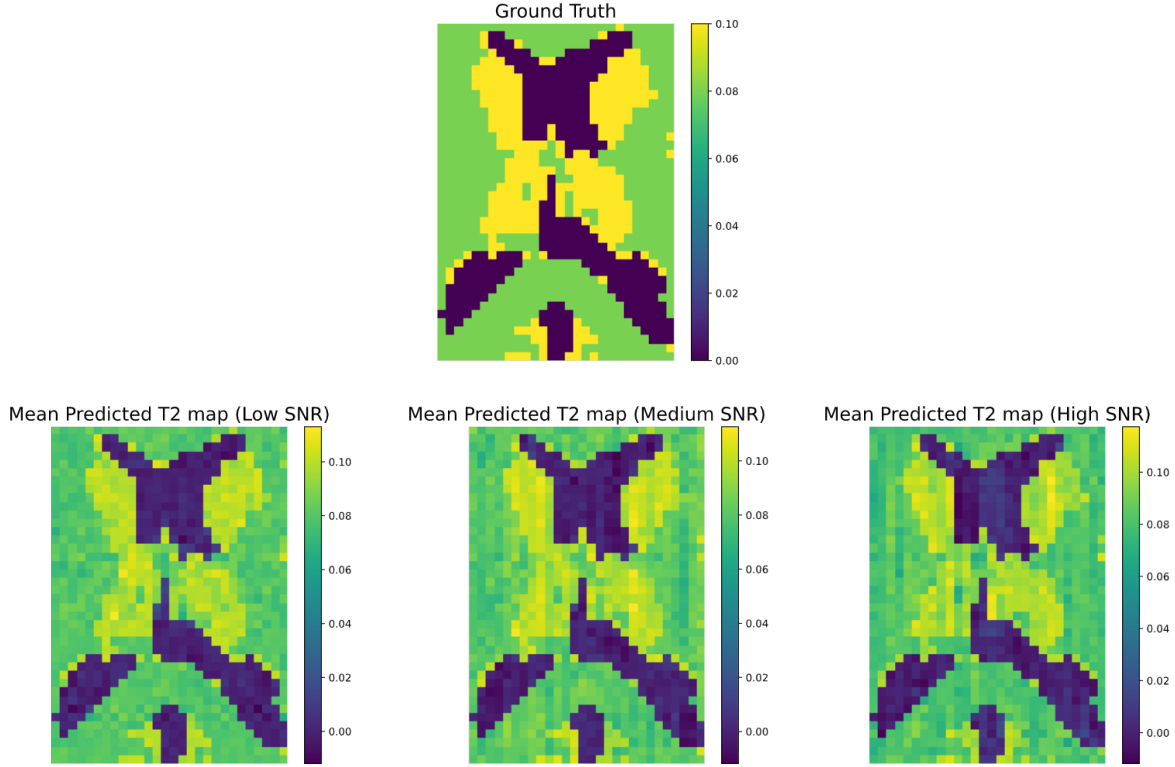


Figure 12: *Ground truth  $T_2$  map (top) ; Mean predicted  $T_2$  maps from 8 phase-cycled bSSFP images in different SNR levels (bottom)*

The mean predicted  $T_2$  maps in all SNR levels are visually similar to the ground truth. The U-Net model is also trained and tested with 6 phase-cycled bSSFP images. The test MSEs are 1.21E-04, 9.08E-05 and 9.20E-05 for low, medium and high SNR respectively, which are higher than their 8 phase cycles counterparts. The mean predicted  $T_2$  maps from 6 phase-cycled bSSFP images in the corresponding SNR levels are obtained (Figure 13).

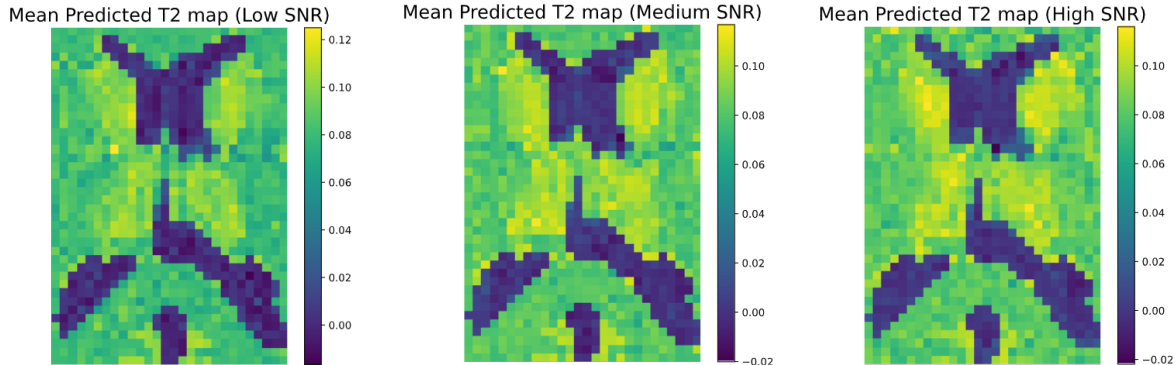


Figure 13: *Mean predicted  $T_2$  maps from 6 phase-cycled bSSFP images in different SNR levels*

In all SNR levels, the U-Net model trained with 6 phase-cycled bSSFP images is able to differentiate between the yellow (GM) and green regions (WM) but the contrast is slightly worse compared to the  $T_2$  maps from 8 phase cycles. This is shown in a significant proportion of  $T_2$  predictions around the midpoint of 80ms and 100ms in the PDFs for 6 phase cycles (See Appendix B). Using fewer phase cycles means that there are less spatial information on parts of the image that are affected by noise and banding artifacts, and so results in ambiguous  $T_2$  estimations.

## 4 Discussion

For 8 and 6 phase-cycled bSSFP input in various SNR levels, voxelwise and image-to-image regression achieve reasonable  $T_2$  predictions, while PLANET is demonstrated to be unfeasible when the SNR is not extremely high ( $< 200$ ). Voxelwise regression performs the best in predicting  $T_2$  from phase-cycled bSSFP signals, which is expected since the ratio of the training data for voxelwise regression to image-to-image regression is 100:1. It is worth noting that the accuracy of image-to-image regression is similar to that of voxelwise regression even with little amount of training data, which shows that the capability to extract spatial information provides great advantage in reconstructing  $T_2$  maps from phase-cycled bSSFP images corrupted with noise and banding artifacts. Overall, both regression networks provides  $T_2$  mapping with significantly higher prediction accuracy and precision than PLANET.

One benefit of predicting  $T_2$  from phase-cycled bSSFP signals using trained regression networks is that it is much faster than PLANET. The possibility of the neural network to work with fewer phase cycles means that bSSFP can acquire sufficient images faster for  $T_2$  mapping, which can tremendously reduce patient scan time and accelerate clinical diagnosis. With better  $T_2$  predictions in low SNR environments, the regression networks also have great potential for  $T_2$  mapping from scan images acquired with low field strength ( $< 1.5T$ ) MRI scanners since interests in low field MRI have resurged due to its low cost and energy efficiency [15][16].

There are several limitations, however, on the current approaches. First, the image-to-image regression supports only  $40 \times 224$  pixels (8 phase cycles) and  $40 \times 168$  pixels (6 phase cycles) images, which needs to be adapted to fit higher resolution images so that the networks can be trained with  $320 \times 320$  pixels defined as the acceptable resolution for clinical MRI scans [17]. One problem that could arise from using such low resolution and limited FOV is that there is a high possibility that the neural networks would not generalize well on phase-cycled bSSFP images with higher resolution and wider FOV. Second, while the simulation of bSSFP dataset is attempted to be as comprehensive as possible, many other artifacts like aliasing, flow, wrap-around, chemical shift, etc. that are routinely encountered in clinical practice are not taken into account. Additionally, Gaussian noise model does not necessarily apply to bSSFP signals of lower SNR ( $< 2$ ) in which the associated noise follows a different distribution called Rician, a narrower Gaussian model [18]. More complex noise models such as non-central chi distribution may also be more appropriate in low SNR regimes [19]. A simulation that mimics actual phase-cycled bSSFP scans more closely is needed to generate higher quality training data for the regression networks.

The flexibility and modularity of the regression networks that account for the limitations should be highlighted. Phase-cycled bSSFP images with different resolutions can be accommodated by tweaking the input, hidden and output layers of the image-to-image regression with desired sizes. The Gaussian noise model and SNR range used in training for both regression networks can be easily swapped out for different noise models and SNRs.

The voxelwise regression is adapted from Yu et al.’s (2020) Model-informed Machine Learning (MIML) method which reconstructs  $T_2$  distribution from 32 echoes of ME-SE with MLP [20]. As with image-to-image regression, no similar work which accelerates  $T_2$  mapping with phase-cycled bSSFP images through CNN is identified during literature review. Established neural networks like Hamilton et al’s (2020) network for rapid  $T_2$  mapping is trained with 8 millions cardiac MR images [21]. In the future, a larger scale of bSSFP data is required to ensure that both regression networks are sufficiently trained and tested. Experiments with phase cycles fewer than 6 will be conducted to investigate the suitability of the current regression networks with shorter phase-cycled bSSFP signals. The feasibility of the regression networks for  $T_2$  mapping for other tissues such as cartilage and myocardium will also be further examined. Other than PLANET, there are several approaches that perform  $T_2$  estimations from phase-cycled bSSFP signals. Björk et al. (2013) designed an algorithm named LORE-GN that estimates  $T_2$  based on a robust linearizing approach [22]. Nguyen and Bieri (2017) developed a method termed MIRACLE which achieves  $T_2$  mapping from frequency-shifted bSSFP scans [23]. Another approach called CELF which introduces additional geometric constraints to PLANET ellipse fitting to estimate  $T_2$  from bSSFP signals with as few as 4 phase cycles, is recently proposed by Keskin et al. (2021) [24]. Moving forward, it will be useful to compare the current regression networks with methods like LORE-GN, MIRACLE and CELF.

## 5 Conclusion

In this work, two different implementations of neural network for  $T_2$  mapping using phase-cycled bSSFP signals are presented. The neural networks are trained and test with bSSFP signals of different numbers of phase cycles and SNR levels. Comparisons between the means and standard deviations of predicted  $T_2$  from voxelwise regression, image-to-image regression and PLANET are conducted across a wide range of SNR. Through evaluation on simulated data, the neural networks are shown to outperform PLANET in SNR levels. Nevertheless, further improvements such as simulating more realistic phase-cycled bSSFP signals, training with larger scale of data and modifications for higher resolution images are necessary for future experiments with actual MRI scans and clinical deployment. In summary, the project lays a solid groundwork for deep learning application in rapid and robust  $T_2$  mapping using phase-cycled bSSFP signals.

## 6 References

- [1] T. Baum et al. “Cartilage and meniscal T2 relaxation time as non-invasive biomarker for knee osteoarthritis and cartilage repair procedures”. In: *Osteoarthritis and Cartilage* 21.10 (2013), pp. 1474–1484. ISSN: 1063-4584. DOI: <https://doi.org/10.1016/j.joca.2013.07.012>. URL: <http://www.sciencedirect.com/science/article/pii/S1063458413008984>.
- [2] Xiaojuan Li et al. “In vivo T(1RHO) and T(2) mapping of articular cartilage in osteoarthritis of the knee using 3T MRI”. In: *Osteoarthritis and cartilage / OARS, Osteoarthritis Research Society* 15 (Aug. 2007), pp. 789–97. DOI: <10.1016/j.joca.2007.01.011>.
- [3] T.-C Chuang et al. “Banding artifacts along the frequency-encoding direction in multi-echo magnetic resonance imaging: Origin and a remedy”. In: *Journal of Medical and Biological Engineering* 24 (June 2004), pp. 69–75.
- [4] Qing-San Xiang and Michael N. Hoff. “Banding artifact removal for bSSFP imaging with an elliptical signal model”. In: *Magnetic Resonance in Medicine* 71.3 (2014), pp. 927–933. DOI: <https://doi.org/10.1002/mrm.25098>. URL: <https://onlinelibrary.wiley.com/doi/abs/10.1002/mrm.25098>.
- [5] Yulia Shcherbakova et al. “PLANET: An ellipse fitting approach for simultaneous T1 and T2 mapping using phase-cycled bSSFP”. In: *Magnetic Resonance in Medicine* 79.2 (2018), pp. 711–722. DOI: <https://doi.org/10.1002/mrm.26717>. URL: <https://onlinelibrary.wiley.com/doi/abs/10.1002/mrm.26717>.
- [6] Ziyu Meng et al. “Accelerating T2 mapping of the brain by integrating deep learning priors with low-rank and sparse modeling”. In: *Magnetic Resonance in Medicine* 85.3 (2020), pp. 1455–1467. DOI: <10.1002/mrm.28526>.
- [7] Jiaxin Zhao. *Development of bSSFP Simulation and Evaluation of PLANET Mapping*. Imperial College London, 2020.
- [8] Sahar Hassani et al. “Degrees of freedom estimation in Principal Component Analysis”. In: 118 (Aug. 2012), pp. 246–259. DOI: <10.1016/j.chemolab.2012.05.015>.
- [9] *BrainWeb: 20 Anatomical Models of 20 Normal Brains*. URL: [https://brainweb.bic.mni.mcgill.ca/cgi/brainweb1?alias=subject20\\_crisp](https://brainweb.bic.mni.mcgill.ca/cgi/brainweb1?alias=subject20_crisp).
- [10] S. Siemonsen et al. “Age-Dependent Normal Values of T2\* and T2 in Brain Parenchyma”. In: *American Journal of Neuroradiology* 29.5 (2008), pp. 950–955. DOI: <10.3174/ajnr.a0951>.
- [11] Revital Nossin-Manor et al. “Optimized T1- and T2-weighted volumetric brain imaging as a diagnostic tool in very preterm neonates”. In: *Pediatric Radiology* 41.6 (2010), pp. 702–710. DOI: <10.1007/s00247-010-1955-5>.
- [12] Janaka P. Wansapura et al. “NMR relaxation times in the human brain at 3.0 tesla”. In: *Journal of Magnetic Resonance Imaging* 9.4 (1999), pp. 531–538. DOI: [10.1002/\(sici\)1522-2586\(199904\)9:4<531::aid-jmri4>3.0.co;2-1](10.1002/(sici)1522-2586(199904)9:4<531::aid-jmri4>3.0.co;2-1).
- [13] Michael J. Knight et al. “Quantitative T1 and T2 MRI signal characteristics in the human brain: different patterns of MR contrasts in normal ageing”. In: *Magnetic Resonance Materials in Physics, Biology and Medicine* 29.6 (2016), pp. 833–842. DOI: <10.1007/s10334-016-0573-0>.

- [14] Brian Hargreaves. Signal-to-Noise Ratio - Single-Channel Noise and SNR Measurement. URL: [https://web.stanford.edu/class/rad229/Notes/Lecture-07/Rad229\\_2020\\_Lecture07A\\_SingleChannelSNR.pdf](https://web.stanford.edu/class/rad229/Notes/Lecture-07/Rad229_2020_Lecture07A_SingleChannelSNR.pdf).
- [15] José P. Marques, Frank F.j. Simonis, and Andrew G. Webb. “Low-field MRI: An MR physics perspective”. In: Journal of Magnetic Resonance Imaging 49.6 (2019), pp. 1528–1542. DOI: 10.1002/jmri.26637.
- [16] Mathieu Sarracanie and Najat Salameh. Low-Field MRI: How Low Can We Go? Apr. 2020. URL: <https://www.frontiersin.org/articles/10.3389/fphy.2020.00172/full>.
- [17] MRI resolution and image quality: how to manipulate mri scan parameters. URL: <https://mrimester.com/index.4.html>.
- [18] H. Gudbjartsson and S. Patz. “The rician distribution of noisy mri data”. In: Magnetic Resonance in Medicine 34.6 (1995), pp. 910–914. DOI: 10.1002/mrm.1910340618.
- [19] Divya Varadarajan and Justin P. Haldar. “A Majorize-Minimize Framework for Rician and Non-Central Chi MR Images”. In: IEEE Transactions on Medical Imaging 34.10 (2015), pp. 2191–2202. DOI: 10.1109/tmi.2015.2427157.
- [20] Thomas Yu et al. “Model-Informed Machine Learning for Multi-component T2 Relaxometry”. In: (July 2020).
- [21] Jesse I. Hamilton et al. “Deep learning reconstruction for cardiac magnetic resonance fingerprinting T1 and T2 mapping”. In: Magnetic Resonance in Medicine (). DOI: <https://doi.org/10.1002/mrm.28568>. URL: <https://onlinelibrary.wiley.com/doi/abs/10.1002/mrm.28568>.
- [22] Marcus Björk et al. “Parameter estimation approach to banding artifact reduction in balanced steady-state free precession”. In: Magnetic Resonance in Medicine 72.3 (2013), pp. 880–892. DOI: 10.1002/mrm.24986.
- [23] Damien Nguyen and Oliver Bieri. Motion-insensitive rapid configuration relaxometry. Aug. 2017. URL: <https://www.ncbi.nlm.nih.gov/pubmed/27605508>.
- [24] K. Keskin et al. Constrained ellipse fitting for efficient parameter mapping with phase-cycled bSSFP. 2021. arXiv: 2106.03239 [eess.IV].

# Appendix

## A Functions of the layers used for image-to-image regression

### Convolutional layer

Convolutional layers apply a convolution operation defined by kernel size to the input, passing the result to the next layer. A convolution converts all the pixels within the kernel into a single value in the successive layer

### Batch Normalisation layer

Batch normalization applies a transformation that maintains the mean output close to 0 and the output standard deviation close to 1 to mitigate internal covariate shift, meaning to ensure that the input for every layer is distributed around the same mean and standard deviation, and thus stabilize and speed up training.

### Max Pooling layer

Maximum pooling, or max pooling, is a pooling operation that calculates the largest value in each patch of each feature map. Using max pooling layers creates down sampled or pooled feature maps that highlight the most present feature in the patch.

### Transposed Convolution layer

A transposed convolutional layer carries out reverse convolution, or deconvolutions to upsample feature maps.

### Concatenating layer

A concatenating layer takes inputs and concatenates them along a specified dimension. The inputs must have the same size in all dimensions except the dimension in which concatenation takes place.

## B PDFs for 6 phase cycles

### Voxelwise Regression

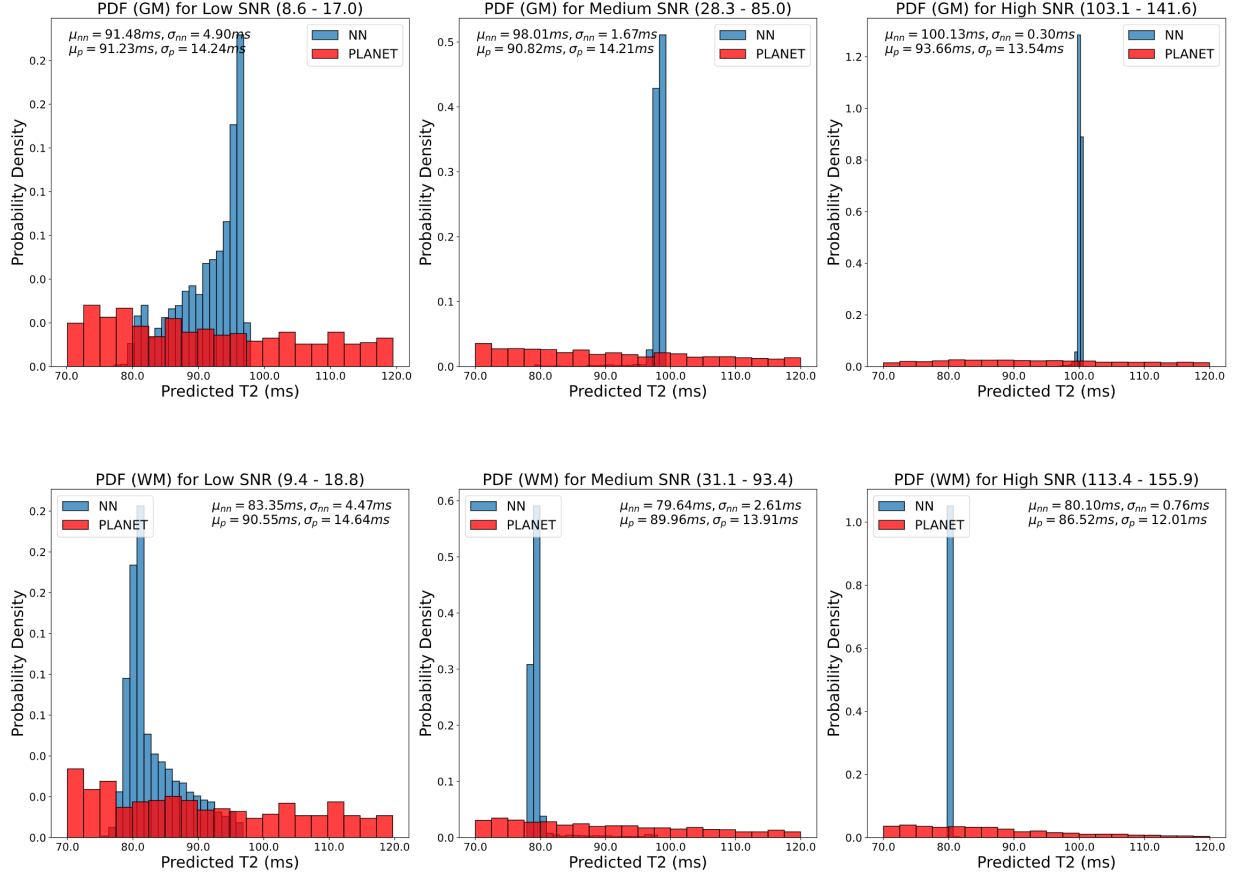


Figure 15: *GM and WM PDFs of predicted T<sub>2</sub> from PLANET (red) and voxelwise regression (blue) for 6 phase-cycled bSSFP signals in different SNR levels*

## Image-to-image Regression

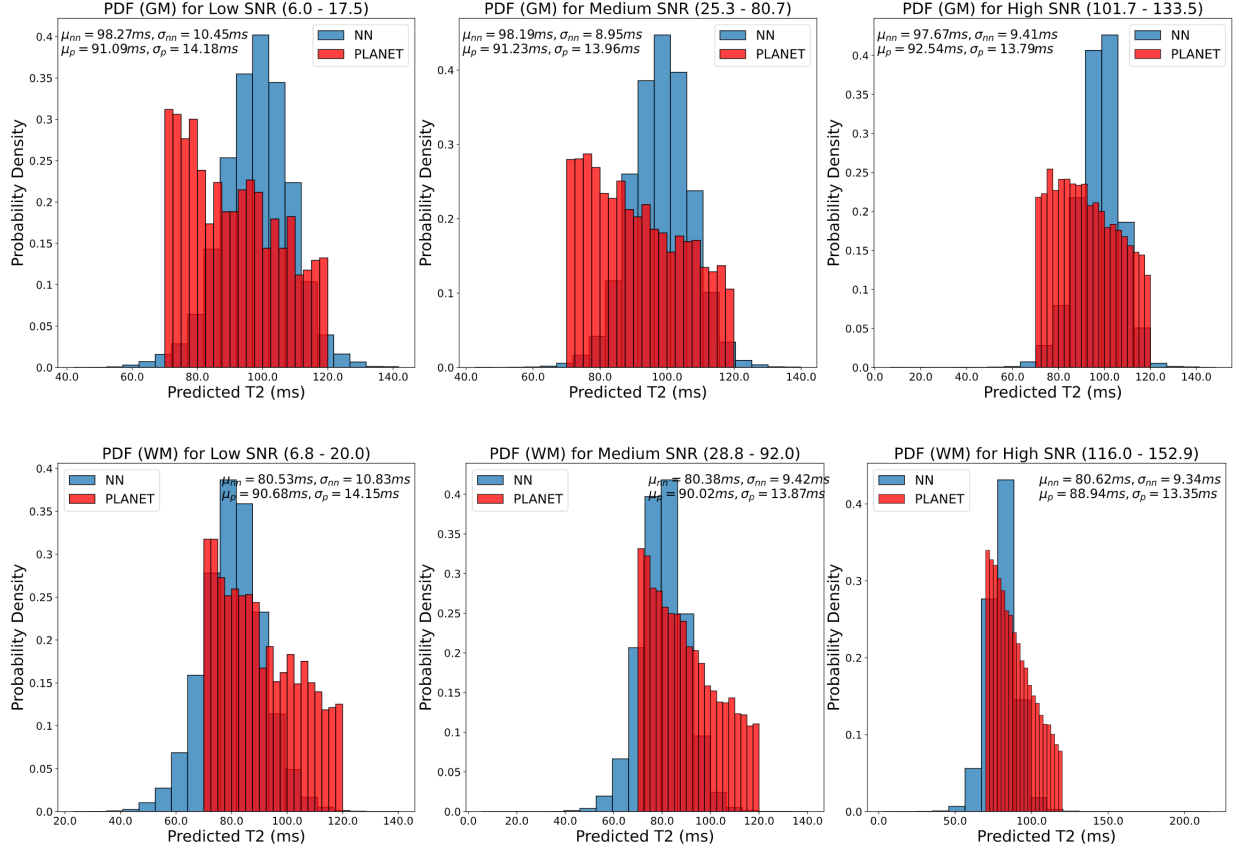


Figure 17: GM and WM PDFs of predicted  $T_2$  from PLANET (red) and image-to-image regression (blue) for 6 phase-cycled bSSFP images in different SNR levels